inorganics

MDPI

Article

Luminescence Study of Hydrogenated Silicon Oxycarbide (SiO_xC_y:H) Thin Films Deposited by Hot Wire Chemical Vapor Deposition as Active Layers in Light Emitting Devices

Juan R. Ramos-Serrano [1], Yasuhiro Matsumoto [2], Alejandro Ávila [2], Gabriel Romero [2], Maricela Meneses [2], Alfredo Morales [1], José A. Luna [3], Javier Flores [4,5], Gustavo M. Minquiz [4,5] and Mario Moreno-Moreno [1,*]

1 Electronics Coordination, Instituto Nacional de Astrofísica, Óptica y Electrónica, Tonantzintla, Puebla 72840, Mexico; juan.ramos@inaoep.mx (J.R.R.-S.); alfredom@inaoep.mx (A.M.)
2 Electrical Engeneering Department, Centro de Investigación y de Estudios Avanzados del IPN, Mexico City 07360, Mexico; ymatsumo@cinvestav.mx (Y.M.); aavila@cinvestav.mx (A.Á.); gromero@cinvestav.mx (G.R.); marmem369@gmail.com (M.M.)
3 Centro de Investigaciones en Dispositivos Semiconductores (CIDS-ICUAP), Benemérita Universidad Autónoma de Puebla (BUAP), Col. San Manuel, Cd. Universitaria, Av. San Claudio y 14 Sur, Edificios IC5 y IC6, Puebla 72570, Mexico; jose.luna@correo.buap.mx
4 Ingeniería Mecánica, Tecnológico Nacional de México/I.T. Puebla, Av. Tecnológico #420 Col. Maravillas, Puebla 72220, Mexico; javier.flores@puebla.tecnm.mx (J.F.); gminquiz@yahoo.com (G.M.M.)
5 Área de Ingeniería, Benemérita Universidad Autónoma de Puebla, Ciudad Universitaria, Blvd. Valsequillo y Esquina Av. San Claudio s/n, Col. San Manuel, Puebla 72570, Mexico
* Correspondence: mmoreno@inaoep.mx; Tel.: +52-(222)-266-31-00

Abstract: The obtention of luminescent SiO_xC_y:H thin films deposited by the HW-CVD technique is reported here. We study the effect of different monomethyl-silane (MMS) flow rates on the films properties. An increase in the emission bandwidth and a red-shift was observed when the MMS flow increased. The luminescence was related to optical transitions in band tail states and with less contribution from quantum confinement effects. After, the films were annealed at 750 °C in nitrogen. The annealed film deposited at the highest MMS flow showed an emission spectrum like the as-deposited film, suggesting the same emission mechanisms. By contrast, the annealed film deposited at the lowest MMS flow showed two emission bands. These bands are due to the activation of radiative defects related to oxygen-deficient centers. MOS-like structures were fabricated as electroluminescent devices using the annealed films. Only the structure of the film with the highest carbon content showed light emission in a broad band in the visible spectrum region in forward bias, with a maximum centered close to 850 nm. The light emission mechanism was related to electron thermalization in the band tail states and a direct hole injection into deep states. The trap-assisted tunneling, Poole–Frenkel emissions and Fowler–Nordheim tunneling were proposed as the charge transport mechanism.

Keywords: hot wire chemical vapor deposition; monomethyl-silane; SiOxCy:H; electroluminescence

Citation: Ramos-Serrano, J.R.; Matsumoto, Y.; Ávila, A.; Romero, G.; Meneses, M.; Morales, A.; Luna, J.A.; Flores, J.; Minquiz, G.M.; Moreno-Moreno, M. Luminescence Study of Hydrogenated Silicon Oxycarbide (SiO_xC_y:H) Thin Films Deposited by Hot Wire Chemical Vapor Deposition as Active Layers in Light Emitting Devices. *Inorganics* **2024**, *12*, 298. https://doi.org/10.3390/inorganics12110298

Academic Editors: Pengwei Li, Yanfei Zhang and Antonino Gulino

Received: 7 October 2024
Revised: 13 November 2024
Accepted: 16 November 2024
Published: 20 November 2024

1. Introduction

Photonics emerges as an alternative to conventional electronics for digital communications, enabling a greater bandwidth, longer distance connections, and lower energy consumption. Specifically, silicon photonics is related to the ability to emit and detect photons using devices fabricated through processes compatible with the existing silicon–CMOS infrastructure. Currently, some silicon photonic devices are marketed; however, for light-emitting devices they continue using III–V compound-semiconductors. Today, there is a growing interest in research for developing light-emitting sources with silicon-based materials, because this allows a better integration in silicon photonics chip manufacturing, taking advantage of the current silicon–CMOS infrastructure. Nowadays, silicon

oxycarbide has attracted attention as a functional silicon-based material for its potential application in the development of silicon photonics. This is mainly due to the capability to modify its optical properties by changing the oxygen–carbon ratio. It has been reported that silicon oxycarbide displays an intense photoluminescence in a wide range of the visible spectrum by modifying the above relationship [1]. On the other hand, low-loss optical waveguides have been developed using the capability to adjust the refractive index to values between those obtained for silicon dioxide and silicon carbide (1.5–2.3), by changing the oxygen–carbon ratio [2].

Chemical vapor deposition (CVD) is a widely used technique for a great variety of high-quality thin films, including silicon-based materials such as hydrogenated amorphous silicon (a-Si:H), silicon carbide (SiC), silicon oxide (SiO_x), and silicon nitride (SiN_x) [3–5]. There are different CVD configurations according to the energy source to produce the dissociation of gas species and promote reactions. Among these processes are the thermal energy source in conventional furnaces, atmospheric pressure CVD (AP-CVD) and low pressure CVD (LP-CVD); plasma enhanced CVD (PE-CVD) is also widely used, where plasma is the source of energy, along with hot wire CVD (HW-CVD), which is used to chemically decompose the precursors [6].

Specifically, the HW-CVD technique has aroused interest in silicon-based material deposition for its simplicity, since it has been reported to obtain nano and microcrystalline phases at low substrate deposition temperatures, as low as 200 °C [7,8]. This work studies the structural and optical properties of hydrogenated silicon oxycarbide (SiO_xC_y:H) thin films. These films were deposited using the HW-CVD technique with a monomethyl-silane (MMS), hydrogen and oxygen mixture, varying only the MMS flow rate. For the electro-optical analysis, MOS-like structures were fabricated using the annealed SiO_xC_y:H films as an active layer.

2. Results and Discussion

Hydrogenated silicon oxycarbide (SiO_xC_y:H) thin films were deposited by the HW-CVD technique using monomethyl-silane (MMS) as a single source of silicon and carbon atoms. The MMS flow rate was varied at 3 and 7 sccm. The films were labeled as S3 and S7, as a reference to the MMS flow. In addition, the films were thermally annealed at 750 °C in nitrogen ($S3_{TA}$, $S7_{TA}$). After the characterization of the films, MOS-like structures were fabricated as electroluminescent devices using the annealed films as active layers because these displayed more intense light emissions than as-deposited films. The deposition parameters, thermal annealing, and MOS-like structure fabrication process are described in Section 3.

2.1. SiO_xC_y:H Thin Films Characterization

X-ray photoelectron spectroscopy (XPS) characterization was carried out to determine the elemental composition and binding configuration. Table 1 shows the elemental composition obtained by XPS for the as-deposited and annealed films. A direct relation between the MMS flow rate and the silicon and carbon content was observed for the as-deposited films. This is due to a greater amount of these within the chamber during the depositions. Rates of tantalum coming from the wire were detected for the S3 film. This is because, at a low MMS flow, the tantalum wire showed quick oxidation related to a low oxygen dilution, where the wire showed a rough surface and was dark gray in color. It is possible to use metallic oxides as solid sources in the HW-CVD technique, in this case Ta_2O_5. This process consists in the generation of atomic hydrogen by the dissociation of molecular hydrogen on the hot wire surface. The atomic hydrogen is highly reactive, inducing first a reduction process and, subsequently, the generation of metal hydrides as gaseous precursors [9]. On the other hand, under the deposition conditions of the S7 film, a protective layer of SiC forms on the wire, showing a smooth surface with a golden color, avoiding the incorporation of tantalum into the films. For the annealed films, a slight reduction in the carbon

content is observed while the oxygen content increases. This may be due to a substitution of the desorbed elemental carbon and CH_n radicals by oxygen atoms.

Table 1. Elemental composition by XPS of the as-deposited and annealed SiOxCy:H films.

Film	Elemental Composition (% atm.)			
	Si	O	C	Ta
S3	39	47	13	1
S7	43	34	23	-
$S3_{TA}$	39	49	11	1
$S7_{TA}$	44	36	20	-

Additionally, from the XPS measurements in the Si2p window, the valence states of the silicon Si^{n+} (n = 0–4) can be determined with the binding energy. For SiO_x films, these states are associated with five possible matrix configurations, which can be expressed as Si-(Si_{4-n}-O_n) with n = 0–4 [10]. However, due to the incorporation of carbon, it is possible to have a great variety of compounds with different stoichiometries. Other authors relate these valence states to the formation of Si-(C_{4-n}-O_n) compounds with n = 0–4 [11]. Because of this, it is difficult to relate the valence states to a single compound in the SiO_xC_y:H matrix. However, for practical purposes, we consider the simplest compounds as a reference. In this case, elemental silicon (Si-Si_4), silicon carbide (Si-C_4) and stoichiometric silicon dioxide (Si-O_4) can be related to Si^0, Si^{+1}, and Si^{+4} valence states, respectively. As another reference, the binding energy increases with higher oxygen content. Figure 1a,b show the XPS spectra in the Si2p window of the S3 and S7 films. In both cases, the spectra show broad bands related to the formation of sub-stoichiometric oxide and silicon oxycarbide compounds, where the main peak placed close to 102.3 eV (S^{+3}) indicates the presence of compounds like Si–Si–O_3 and C–Si–O_3. The silicon oxidation states suggest the presence of oxygen-deficient centers (ODCs) in the SiO_xC_y:H matrix. These ODCs may correspond to several defect-related emission centers. In addition, the spectrum of the S7 film shows a broader band, where, unlike the S3 film, the contribution of s^0 and s^{+1} bands are observed.

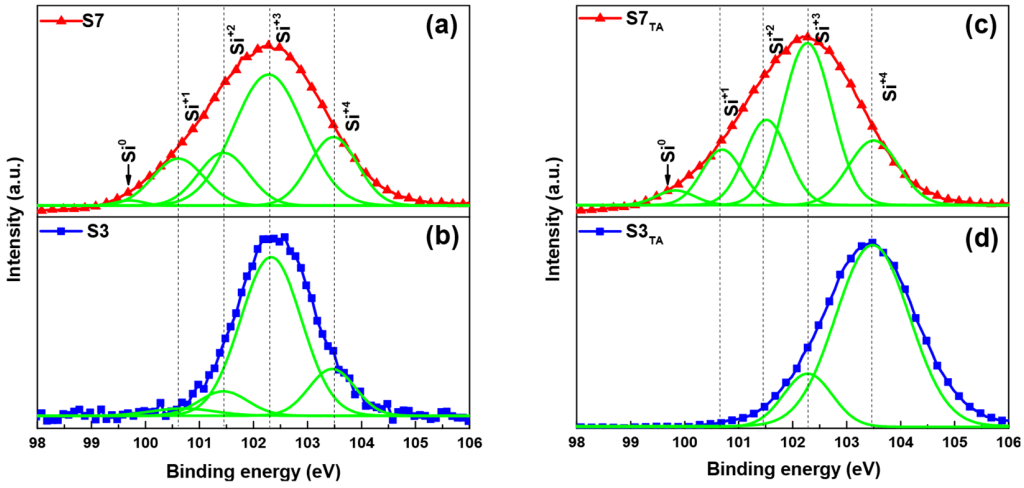

Figure 1. Si2p window in the XPS spectra of the SiO_xC_y:H films (**a**,**b**) as-deposited films and (**c**,**d**) annealed films. The spectra were deconvoluted in components (green lines) related to different silicon valence states.

This indicates that a greater amount of Si–Si and Si–C bonds are formed with increasing MMS flow, which may correspond to the formation of Si/SiC amorphous clusters or nanocrystalline phases. Figure 1c,d show the XPS spectra of the annealed films. The $S3_{TA}$ spectrum shows a shift to a higher binding energy, corresponding to the S^{+4} state. This is due to an increase in the Si–O bonds, where, during the annealing, hydrogen, elemental

carbon and different radicals are desorbed and replaced by oxygen atoms. On the other hand, the $S7_{TA}$ film does not show a shift in the maximum of the spectrum; however, the intensity of the contributions related to S^0 and S^{+1} valence states increase with the annealing. In this case, the result suggests an increase in the amount of Si–Si and Si–C bonds as a result of the higher silicon and carbon content.

Fourier-transform infrared (FTIR) spectroscopy measurements were carried out to provide a more detailed structural analysis of the films. Figure 2a shows the FTIR absorbance spectra of the as-deposited films. Due to the amorphous nature of the host matrix and its complex composition, all films display broad and overlapped spectra. The spectra show absorption bands close to 460, 800, and 1080 cm^{-1} related to rocking, bending and stretching (TO) vibrational modes in Si–O–Si bonds [12]. The stretching absorption band shifts to 1052 and 1041 cm^{-1} for S3 and S7 films, respectively. This shift is directly related to the silicon oxide stoichiometry, where values lower than 1080 cm^{-1} (for stoichiometric SiO_2) indicate the presence of many ODCs due to oxygen vacancies and to the change in the bonding characteristics as a result of carbon incorporation [13,14]. Next to this absorption band, a broad shoulder at around 1100 cm^{-1} is commonly attributed to the Si–O–Si stretching (LO) mode [12]. Close to 920 cm^{-1} appears a broad absorption band related to the stretching vibration of silanol (Si–O–H) groups [15]. The spectra show a lower intensity in this band for the S7 film; this is related to a decrease in the amount of Si–O–H bonds when the MMS flow increases, where a higher carbon content favors the formation of Si–C–H bonds. The absorption band corresponding to the Si–C bonds at 800 cm^{-1} is observed for the S7 film [16]. This is in accordance with the XPS measurements. Other absorption bands related to the Si–CH_3 bonds can also be observed at 1250 cm^{-1} [17]. The presence of this band may be associated with a partial decomposition of the MMS molecule. In addition, the absorption band close to 620 cm^{-1} is related to the formation of tantalum suboxides due to oxidation and subsequent degradation of the tantalum wire [18]. The broadband close to 1600 cm^{-1} corresponds to water, due to the measurements being carried out in environmental conditions [12]. Figure 2b shows the absorbance spectra of the annealed films. In both cases, the absorption band related to CH_3 radicals is no longer present. In addition, a significative reduction in the band related to Si–O–H bonds for the $S3_{TA}$ film can be observed, while for the $S7_{TA}$ film, they do not appear after the thermal annealing.

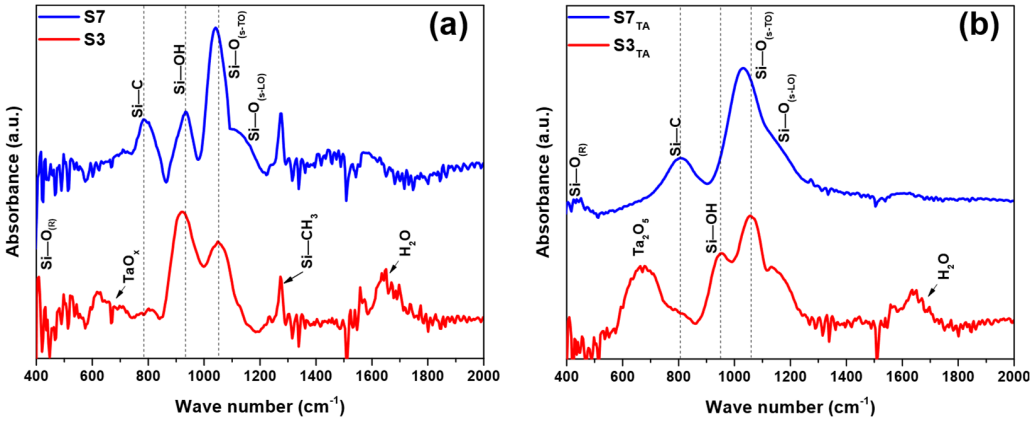

Figure 2. FTIR spectra of the SiO_xC_y:H (**a**) as-deposited films and (**b**) annealed films.

This behavior is related to a desorption process of hydrogen and CH_n radicals. Furthermore, the Si–O–Si stretching absorption band shows a shift to a higher wavenumber related to oxygen incorporation in the $S3_{TA}$ film. The absorption band related to silicon oxide shows a broadening and a shift from 1041 cm^{-1} to 1000 cm^{-1} for the $S7_{TA}$ film. These effects may be attributed to a greater amount of carbon-related bonds in the film. Many reports show that this broadband corresponds to the restructuring of silica materials in different link structures [19].

Figure 3a shows the photoluminescence (PL) spectra of the as-deposited films. The emission intensity for the film obtained at the highest MMS flow rate shows strong luminescence in the visible region, of about 4 times higher than for the film obtained at the lowest MMS flow rate. In addition, a broadening in the emission band and a red-shift in its maximum from 420 nm to 445 nm is observed when the MMS flow rate increases. Due to the material complexity, it is not possible to relate the luminescence origin with a single phenomenon. Among the different luminescent mechanisms are defects-related emissions, quantum confinement effects (QCE), and optical emissions in band tail states. In the case of defects-related emissions, these present emissions at specific wavelengths, so it is impossible to correlate the red-shift and the broadening observed in the emission spectra when the MMS flow rate increases with any particular defect [20]. However, both behaviors can be related to QCE and band tail states. On the one hand, the growth of Si/SiC nanocrystals could give rise to light emissions due to QCE where the increase in the nanocrystal sizes produces a red-shift in the emission wavelength [21]. The presence of nanocrystalline material could not be confirmed by XRD measurements or Raman spectroscopy; however, in a previous study using similar deposition parameters, we reported the obtention of polymorphous SiO_xC_y:H, that is, Si/SiC nanocrystalline phase embedded in an amorphous SiO_xC_y:H host matrix [22]. Considering the above, when the MMS flow increases, it is possible to induce the formation of larger nanocrystals with a broader size distribution, as suggested by the formation of larger clusters observed in the SEM micrographs. On the other hand, in an amorphous semiconductor, there is a continuum of possible states between the valence band and the conduction band, so the energy of the gap is not well defined. This induces the distribution of band tail states due to static disorder. The luminescence band is the result of the distribution of steady-state carriers within these states available for radiative recombination in the band tail [23]. In this case, when the carbon atoms replace the oxygen atoms, the band gap material tends to reduce its energy, producing the red-shift observed [1]. Moreover, the broadening in the emission band as a function of the carbon content may be related to the distribution of the density of band tail states, this is due to an increase in the structural disorder, where the substitution of the Si–Si bond with Si–C and C–C bonds takes place [24]. To have more elements to elucidate the origin of the luminescence in the films, the S3 and S7 films were thermally annealed with the conditions previously described. Figure 3b shows the PL spectra of the $S3_{TA}$ and $S7_{TA}$ films. In both cases, an increase in the emission intensity was observed after the thermal annealing. A remarkable change in the PL spectrum of the $S3_{TA}$ film was noticed. This spectrum displays a significative widening and shows two emission peaks centered in the violet and green regions. We can rule out the changes as a byproduct related to QCE. This is because the conditions in which the thermal annealing was carried out was not enough to induce changes in the fraction of nanocrystalline material, where at least temperatures of 1000 °C and an hour of annealing are required [25]. Nevertheless, the XPS and FTIR results suggest that the origin of these emission bands is related to the activation of luminescent defects in the SiO_xC_y:H matrix due to the desorption of hydrogen and other radicals. In this case, the emission band in the violet region can be associated with oxygen deficiency centers (ODCs), like E′ center, neutral oxygen vacancy (NOV), and the so-called C-related NOV state; while the emission band centered in the green region can be associated with the self-trapped exciton (STE), that is related to wide range luminescence spectra between 2 and 3 eV [26]. The STE is a transient defect, where the electron-hole pair generated after the light excitation can stay bonded by Coulomb forces, forming an exciton with a diameter close to the interatomic distances in Si–O bonds. Some models supports that a hole localized on oxygen and an electron localized on a neighboring silicon result in a small atomic displacement. Further displacement of the oxygen may induce the formation of permanent lattice defects as E′ centers and the non-bridging oxygen hole centers (NBOHC) [27]. Figure 3c shows a schematic diagram of the activation and formation of some of the radiative defects described above. The inset in Figure 3b shows the deconvoluted spectra of the $S3_{TA}$ film. We can observe a contribution from an emission

band centered at 420 nm. This position is the same for the emission band in the as-deposited film, so we can assume that this emission band is related to the same emission mechanism. Considering the conditions for the thermal annealing, the results suggest that the origin of this emission band is related to QCE in the nanocrystalline fraction. On the other hand, for the $S7_{TA}$ film, the maximum of the PL spectra is centered in practically the same position as in the as-deposited film, and it displays a narrowing in the emission band. This may be related, on the one hand, to a reduction in the structural disorder of the film after the annealing induces a reduction in the width of the density distribution of the band tail states, causing a narrowing in the emission band; on the other hand, the emission band may be related to QCE by Si/SiC nanocrystals, since these should not show significant changes under this thermal annealing conditions. Figure 3d shows a schematic band diagram with the different recombination energy levels related to the luminescence in the SiO_xC_y:H films.

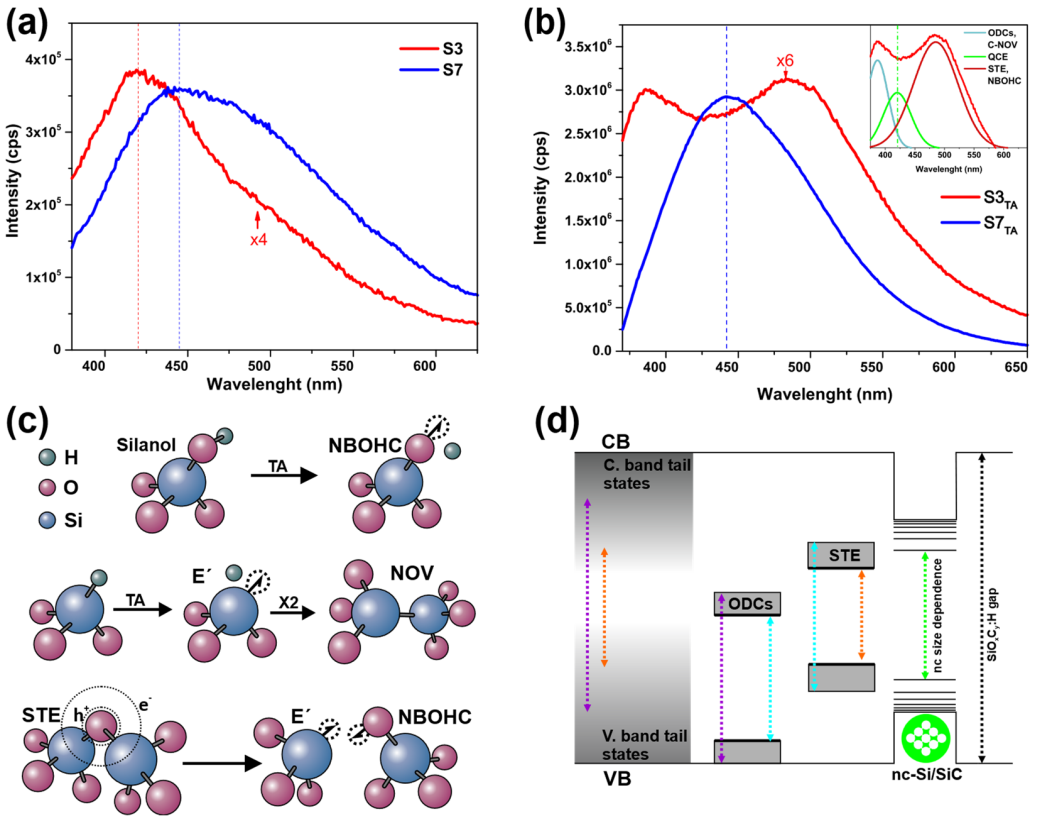

Figure 3. PL spectra of (**a**) as-deposited and (**b**) annealed SiO_xC_y:H films. (**c**) Schematic models of the activation and formation of radiative oxygen-deficient centers. (**d**) Band diagram for the recombination energy levels related to the luminescence in the SiO_xC_y:H films. In (**a**,**b**) dotted lines indicate the wavelength where is the maximum PL emission.

For the implementation of MOS-like electroluminescent structures only the annealed films were used due to these displayed higher PL intensities. Figure 4 shows the scanning electron microscopy (SEM) micrographs of the surface morphology and cross section of the $S3_{TA}$ and $S7_{TA}$ films. Both films show similar granular morphology with the formation of clusters on the surface of a slightly larger size for the $S7_{TA}$ film. A direct relation between the growth rate and the MMS flow was observed, where thicknesses of 40.8 nm and 100.2 nm were measured for samples $S3_{TA}$ and $S7_{TA}$, respectively.

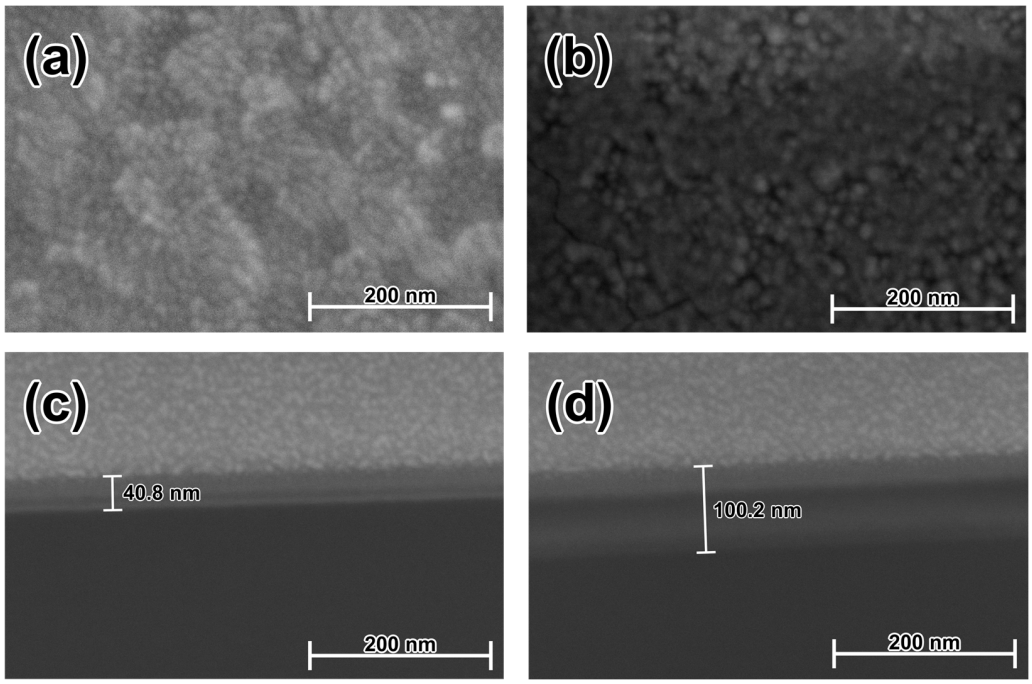

Figure 4. SEM micrographs of the annealed SiOxCy:H films. Surface morphology of (**a**) $S3_{TA}$ and (**b**) $S7_{TA}$. Cross section of (**c**) $S3_{TA}$ and (**d**) $S7_{TA}$.

2.2. Electro-Optical Characterization of Structures

To observe if the implemented structures display electroluminescence (EL), a voltage was applied both in forward bias (FB) and reverse bias (RB), limiting the current to a maximum of 1 mA to avoid damage to structures. Figure 5a shows the EL spectra of the $S3_{TA}$ and $S7_{TA}$ structures with FB voltages of 60 and 55 V, respectively. Only for the $S7_{TA}$ structure in FB, was it possible to see yellow light emissions in the entire area of the device with the naked eye in partial darkness, as we can observe in Figure 5b. The $S7_{TA}$ structure spectra show emissions in a broad band of the NIR-visible region, with a maximum emission close to 860 nm. Compared with the energy of the PL maximum, the EL maximum is notably less. Several authors have reported that in silicon-based materials where the emission is mainly related to QCE or radiative defects, when comparing the PL and EL spectra, they present emission bands with maximums in close positions [28,29]. In our case, the red-shift (~400 nm) could suggest that the EL observed is mainly related to band tail state emissions. Some models for luminescence in amorphous silicon-based materials mention that the red-shift observed is related to a thermalization of the electrons in the conduction band to inter-band tail states with lower energy [30]. Kruangam et al. suggested another reason for this decrease in the emission energy is that the holes are injected directly into the deep states of the gap [31]. The difference between the emission mechanisms of PL and EL is related to the additional process of the injection of carriers, since, while for PL the electron-hole pair is generated simultaneously at the same point in the active layer, the EL carriers are injected at different points of the structure, where their flow is also affected by their mobility in the material and the different barrier heights of the interface where they are injected. Because the mobility of the holes is lower, the carriers' recombination takes place near the c-Si/SiO_xC_y:H interface. This allows the electrons to thermalize, reducing emission energy. On the other hand, in both structures, intense and narrow emission peaks are observed in the blue region. This blue emission appears as bright spots on the surface of the structure, as can be seen in the images in Figure 5b,c. These narrow emission peaks are related to the characteristic radiation of indium ions due to the intense electric field applied to the ITO film [32].

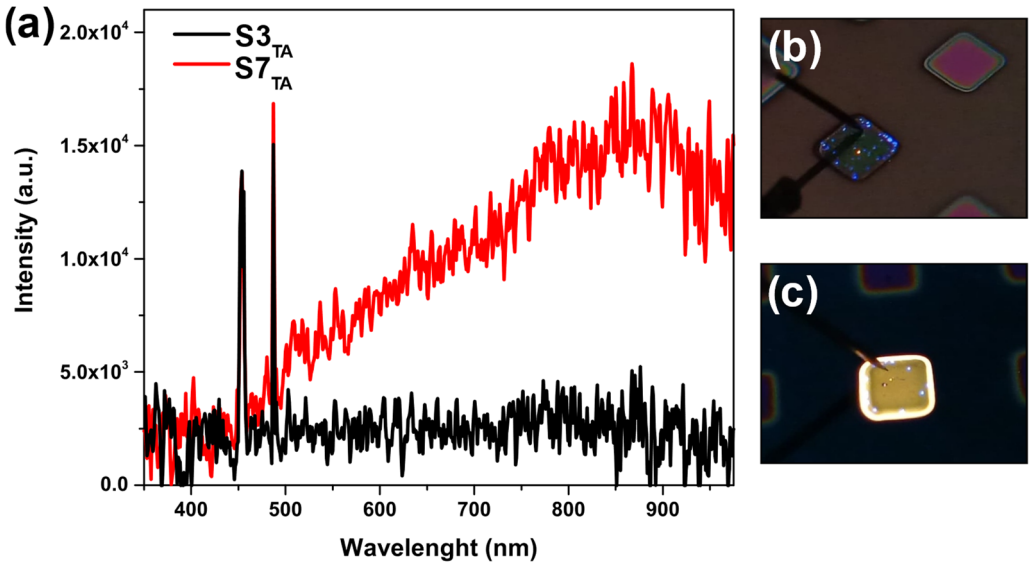

Figure 5. (**a**) Electroluminescence spectra of the $S3_{TA}$ and $S7_{TA}$ structures. (**b**,**c**) EL images of $S3_{TA}$ and $S7_{TA}$ structures, respectively.

To know the electrical properties of the structures, current density-voltage (J-V) characteristics were measured. Figure 6a shows the J-V characteristics in FB and RB of the $S3_{TA}$ and $S7_{TA}$. For both structures in FB, a higher current density is observed. However, the $S7_{TA}$ structure reaches higher current density values for the same FB voltage. This may be related first to a reduction in the gap energy, and then to an increase in the density of localized tail states; both phenomena are due to an increase in the carbon content in the active layer [33]. For low–medium FB voltages, similar current densities are observed in both structures; however, for the $S3_{TA}$ structure there is an abrupt drop in current density. This is related to the annihilation of preferential conductive paths. This is because these paths concentrate a greater current flow, also inducing an increase in temperature due to the Joule effect, causing structural changes for the breaking of Si–Si or Si–O bonds [34].

It is possible to elucidate the electrical charge transport mechanisms in the structure by analyzing the J-V characteristics under different conduction mechanism models. Within these models, those most related to this kind of structure are the Schottky emissions, direct tunneling, Fowler–Nordheim tunneling (F-N), Poole–Frenkel emissions (P-F), and trap-assisted tunneling (TAT) [35]. Only the structure that displayed EL ($S7_{TA}$) was analyzed under these models to identify the charge transport mechanisms. For the low–medium voltage region, the obtained J-V data fitted with the P-F and TAT models. Among the conduction mechanisms, the P-F emissions and TAT are considered as Bulk-limited conduction mechanisms, because the charge transport depends only on the electrical properties of the dielectric itself as the trap energy level, spacing, and density of these. P-F emissions occur in low–medium electric fields. This mechanism involves an electron in a trapping center in the dielectric film where this may be thermally excited out of the trap due to the reduction of the Coulomb potential energy of the electron by the applied electric field, enabling the conduction between localized states. The current density due to P-F emissions is given by Equation (1), where μ is the electronic drift mobility, ε_i and ε_0 are the dielectric constant and the permittivity in vacuum, respectively, N_c is the density of states in the conduction band, E is the electric field and the term ϕ_T is the trap energy level.

$$J_{P-F} = q\mu N_C E\, exp\left[\frac{-q\left(\phi_T - \sqrt{qE/\pi\varepsilon_i\varepsilon_0}\right)}{kT}\right] \quad (1)$$

As with P-F emissions, TAT tunneling involves an electron in a trapping center, where it may tunnel through the dielectric to reach the conduction band. The TAT mechanism also takes place in low–medium electric fields. The current density due to TAT emissions is given by Equation (2), where m_T^* is the tunneling effective mass in the dielectric and the other notations are the same as defined before.

$$J_{TAT} = exp\left[\frac{-8\pi\left(2qm_T^*\right)^{1/2}}{3hE}\phi_T^{3/2}\right] \quad (2)$$

Figure 6b shows the experimental J-V data fitted with the P-F and TAT models, according to Equations (1) and (2), respectively.

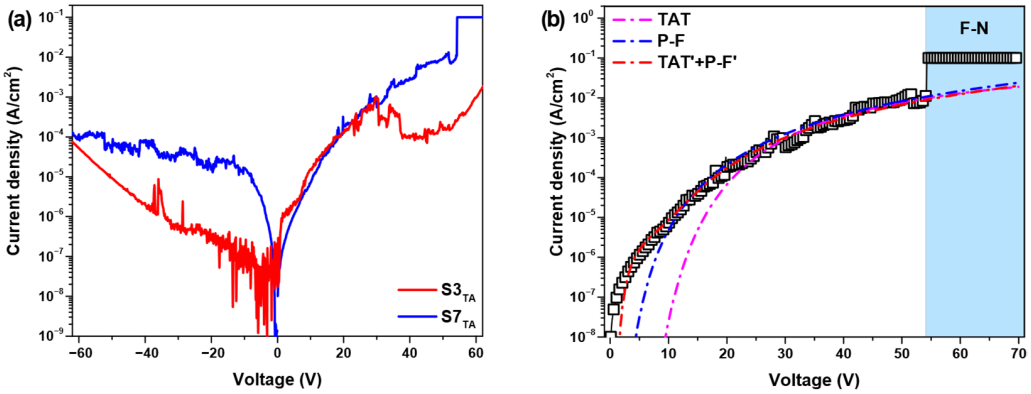

Figure 6. (**a**) Current density-voltage characteristics of the $S3_{TA}$ and $S7_{TA}$ structures in FB and RB. (**b**) J-V characteristic of the $S7_{TA}$ structure fitted to TAT and P-F conduction mechanism.

Both models show a fit with the J-V curve at the medium electric field region; however, the P-F model shows a better fit at the low electric field region. Considering that different conduction mechanisms can contribute to the conduction current through the dielectric simultaneously, a joint fit of both models was carried out, i.e., P-F' + TAT'. We can observe a complete fit with the J-V curve. In this, two regions can be distinguished, the first for <10 V corresponds to P-F emissions, and the second for >10 V corresponds to the TAT. These results are related to a high density of localized tail states in the SiO_xC_y:H film. Due to the limited maximum current, it was impossible to identify the conduction mechanism for the high electric field region by comparing the J-V data with any model. However, in similar MOS-like structures, several authors report that the predominant conduction mechanism at high electric fields is F-N tunneling [36,37]. This mechanism is considered an electrode-limited conduction mechanism, where the barrier height at the electrode–dielectric interface is the most important parameter. F-N tunneling takes place when a high electric field induces the formation of a triangular potential barrier, narrow enough (<10 nm) for electrons to pass through into the conduction band of the dielectric because of the tunneling effect. Finally, based on the obtained results, Figure 7 shows the band diagram proposed for EL and the charge transport mechanism.

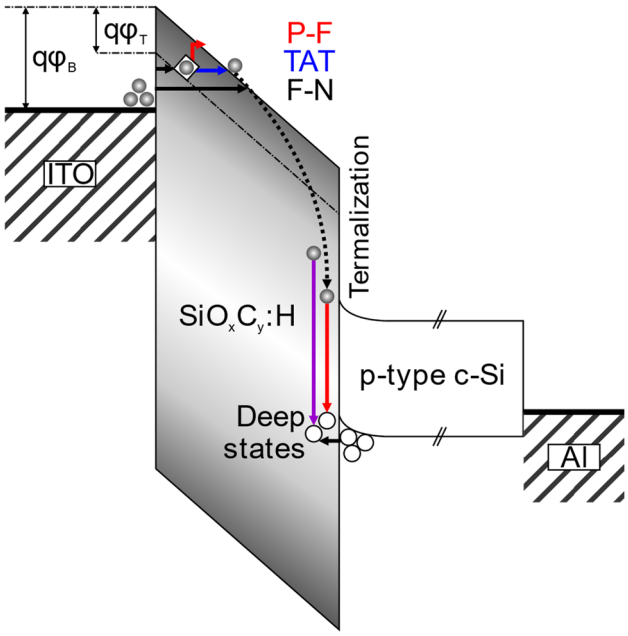

Figure 7. Schematic energy band diagram of the $S7_{TA}$ structure showing the EL and electrical conduction mechanism in FB condition.

3. Materials and Methods

3.1. Sample Preparation

Hydrogenated silicon oxycarbide (SiOxCy:H) thin films were deposited on p-type polished silicon substrates (100) with a resistivity of 1–4 Ω·cm by the HW-CVD technique. As catalyst material a 0.5 mm-diameter tantalum (Ta) wire at 1800 °C located 50 mm above the substrate was used. Hydrogen, oxygen, and MMS (purity 99.9%) were used as reactant gases. The hydrogen and oxygen flow rates were fixed at 20 sccm and 1 sccm, respectively, while the MMS flow rate was varied at 3 and 7 sccm (S3, S7). The films deposition maintained the substrate temperature at 200 °C and the chamber pressure at 0.1 Torr for 30 min. After deposition, the films were thermally annealed at 750 °C in nitrogen at atmospheric pressure for 30 min ($S3_{TA}$, $S7_{TA}$). After the characterization of the films, MOS-like structures were fabricated as electroluminescent devices using the annealed SiOxCy:H films as an active layer. A 100 nm thick indium thin oxide (ITO) film was deposited onto the $S3_{TA}$ and $S7_{TA}$ films by RF sputtering technique with a power of 60 W at room temperature, which was used as transparent contact. Then, 1 mm^2 square-shaped patterns were defined on the ITO contact. On the back side of the c-Si substrate, an approximately 1 μm thick aluminum layer was deposited by thermal evaporation. Finally, the structures were thermally annealed at 350 °C in a vacuum for 30 min to improve contact quality.

3.2. Characterization

The elemental composition of the films and the silicon chemical state were analyzed by X-ray photoelectron spectroscopy (XPS) in a system model K-Alpha (Thermo Scientific, Waltham, MA, USA) with an Al-Kα source. A Fourier-transform infrared spectrometer (FTIR) model Nicolet- iS50 (Thermo Scientific, Waltham, MA, USA), was used in a transmittance configuration in a range of 400–2000 cm^{-1} with a resolution of 4 cm^{-1}. The samples consisted of SiOxCy:H films deposited on c-Si substrates. Also, a clean c-Si substrate from the same wafer used for the films deposition was used to subtract the background signal from the absorbance spectra of the thin films. Photoluminescence (PL) spectra were obtained at room temperature in a Nanolog spectrometer from Horiba Jobin Yvon (Horiba Ltd., Kioto, Japan), using an excitation wavelength of 350 nm from a 450 W Xe-lamp. Surface morphology and cross-section micrographs were obtained by scanning

electron microscopy (SEM) FEI Scios (Thermo Scientific, Waltham, MA, USA). To study the electro-optical properties of the SiO_xC_y:H based structures, the current density-voltage (J-V) characteristic was measured in a 4200-SCS parameter analyzer (Keithley, Solon, OH, USA), while the electroluminescence spectra were collected with an optical fiber coupled in a Horiba Duetta spectrometer (Horiba Ltd., Kioto, Japan).

4. Conclusions

The properties of SiO_xC_y:H thin films at different MMS flow rate were studied. A direct relation between the intensity and the width of the emission band with the carbon content in the films was observed. Also, a red-shift from 408 nm to 445 nm occurred when the MMS flow rate was increased. This shift and the broadening of the emission band suggest that luminescence is caused by optical transitions in band tail states with less contribution from QCEs in the nanocrystalline fraction. The annealed film $S7_{TA}$ showed a narrowing in the emission band; however, the emission maximum position remained the same. This suggests that the emission mechanisms are the same for the as-deposited film. On the other hand, the annealed film $S3_{TA}$ showed two emission bands centered in the violet and green regions, respectively. This was related to radiative defects in the SiO_xC_y:H matrix, due to the activation of different oxygen-deficient centers by the desorption of hydrogen and other radicals. Electroluminescent structures were implemented with the annealed films. Both structures displayed shiny blue dots on the surface related to the characteristic radiation of indium ions. Only the $S7_{TA}$ structure displayed an intense emissions in the entire area of yellow color when a 55 V FB was applied. The EL emission band showed a red-shift of about 400 nm with respect to the PL maximum. This is because the holes are injected into the deep band tail states and the electrons in the conduction band begin to lose energy as they move through the active layer due to the thermalization process. On the other hand, for this structure, the carriers conduction may be related first to the P-F emissions and the TAT due to a high density of band tail states, and second to F-N at high electric fields where the electrons can tunnel the triangular potential barrier to the conduction band.

Author Contributions: Conceptualization, J.R.R.-S. and Y.M.; methodology, J.R.R.-S., A.Á., G.R. and M.M.; validation A.Á., G.R. and M.M.; resources, J.R.R.-S., Y.M., A.M. and M.M.-M.; writing—original draft preparation, J.R.R.-S., Y.M., A.Á., G.R. and M.M.-M.; writing—review and editing, A.M., J.A.L., J.F. and G.M.M.; visualization, J.R.R.-S. and Y.M.; supervision, A.M., M.M.-M. and J.A.L.; project administration, J.R.R.-S., Y.M. and M.M.-M.; funding acquisition, J.R.R.-S., Y.M., J.A.L., M.M.-M., J.F. and G.M.M. All authors have read and agreed to the published version of the manuscript.

Funding: This research received no external funding.

Data Availability Statement: The original contributions presented in this study are included in the article. Further inquiries can be directed to the corresponding author.

Acknowledgments: J. R. Ramos-Serrano acknowledges CONAHCYT for the scholarship granted. The authors thank A. Mendez-Blas from IFUAP for PL measurements. We also appreciate Netzahualcoyotl Carlos Ramírez for SEM characterizations. We would like to express our sincere thanks to I. A. Oliva from the CINVESTAV-Mérida Unit for the XPS measurements. The authors thank Miguel A. Luna, Miguel Galván and Norma I. González from SEES-CINVESTAV for their technical assistance.

Conflicts of Interest: The authors declare no conflicts of interest.

References

1. Lin, Z.; Guo, Y.; Song, C.; Song, J.; Wang, X.; Zhang, Y.; Huang, R.; Huang, X. Influence of the Oxygen Content in Obtaining Tunable and Strong Photoluminescence from Low-Temperature Grown Silicon Oxycarbide Films. *J. Alloys Compd.* **2015**, *633*, 153–156. [CrossRef]
2. Baudzus, L.; Krummrich, P.M. Low-Loss Planar Optical Waveguides Based on Plasma Deposited Silicon Oxycarbide. *Opt. Mater. Express* **2019**, *9*, 2797. [CrossRef]
3. Matsumoto, Y. Hot Wire-CVD Deposited a-SiOx and Its Characterization. *Thin Solid Films* **2006**, *501*, 95–97. [CrossRef]

4. Nakayama, H.; Hata, T. Low-Temperature Growth of Si-Based Organic-Inorganic Hybrid Materials, Si-O-C and Si-N-C, by Organic Cat-CVD. *Thin Solid Films* **2006**, *501*, 190–194. [CrossRef]
5. Stannowski, B.; Rath, J.K.; Schropp, R.E.I. Growth Process and Properties of Silicon Nitride Deposited by Hot-Wire Chemical Vapor Deposition. *J. Appl. Phys.* **2003**, *93*, 2618–2625. [CrossRef]
6. Carlsson, J.-O.; Martin, P.M. Chemical Vapor Deposition. In *Handbook of Deposition Technologies for Films and Coatings*; Elsevier: Amsterdam, The Netherlands, 2010; pp. 314–363, ISBN 9780815520313.
7. Matsumoto, Y.; Godavarthi, S.; Ortega, M.; Sánchez, V.; Velumani, S.; Mallick, P.S. Size Modulation of Nanocrystalline Silicon Embedded in Amorphous Silicon Oxide by Cat-CVD. *Thin Solid Films* **2011**, *519*, 4498–4501. [CrossRef]
8. Finger, F.; Astakhov, O.; Bronger, T.; Carius, R.; Chen, T.; Dasgupta, A.; Gordijn, A.; Houben, L.; Huang, Y.; Klein, S.; et al. Microcrystalline Silicon Carbide Alloys Prepared with HWCVD as Highly Transparent and Conductive Window Layers for Thin Film Solar Cells. *Thin Solid Films* **2009**, *517*, 3507–3512. [CrossRef]
9. Benítez-Lara, A.; García-Salgado, G.; Vázquez-Valerdi, D.E.; Morales-Sánchez, A.; Espinosa-Torres, N.D.; Luna-López, J.A. Silicon Rich Oxide Powders by HWCVD: Its Optical and Morphological Properties. *Adv. Powder Technol.* **2015**, *26*, 163–168. [CrossRef]
10. Palacios-Huerta, L.; Cabañas-Tay, S.A.; Cardona-Castro, M.A.; Aceves-Mijares, M.; Domínguez-Horna, C.; Morales-Sánchez, A. Structural and Optical Properties of Silicon Rich Oxide Films in Graded-Stoichiometric Multilayers for Optoelectronic Devices. *Appl. Phys. Lett.* **2016**, *109*, 031906. [CrossRef]
11. Xu, H.; Wang, Q.; Xiao, H.; Li, X.; Su, X.; Tang, M.; Chen, L.; Li, S. In Situ Preparation of C-SiC x O y Coatings with Controllable Composition on Continuous Oxygen-Enriched SiC Fibres. *RSC Adv.* **2019**, *9*, 1319–1326. [CrossRef]
12. Basu, S. *Crystalline Silicon—Properties and Uses*; Basu, S., Ed.; IntechOpen: London, UK, 2011; ISBN 978-953-307-587-7.
13. Yang, C.S.; Yu, Y.H.; Lee, K.M.; Lee, H.J.; Choi, C.K. Investigation of Low Dielectric Carbon-Doped Silicon Oxide Films Prepared by PECVD Using Methyltrimethoxysilane Precursor. *Thin Solid Films* **2006**, *506–507*, 50–54. [CrossRef]
14. Carneiro, J.O.; Machado, F.; Rebouta, L.; Vasilevskiy, M.I.; Lanceros-Méndez, S.; Teixeira, V.; Costa, M.F.; Samantilleke, A.P. Compositional, Optical and Electrical Characteristics of SiOx Thin Films Deposited by Reactive Pulsed DC Magnetron Sputtering. *Coatings* **2019**, *9*, 468. [CrossRef]
15. Wang, S.; Ji, L.; Li, L.; Wu, Y.; Zhang, Y.; Lin, Z. Selective 6H-SiC White Light Emission by Picosecond Laser Direct Writing. *Sci. Rep.* **2018**, *8*, 257. [CrossRef]
16. Costantini, J.-M.; Miro, S.; Pluchery, O. FTIR Study of Silicon Carbide Amorphization by Heavy Ion Irradiations. *J. Phys. D. Appl. Phys.* **2017**, *50*, 095301. [CrossRef]
17. Kim, C.Y.; Lee, H.S.; Choi, C.K.; Yu, Y.H.; Navamathavan, R.; Lee, H.J. Method of Sealing Pores in Porous Low-k SiOC(-H) Films Fabricated Using Plasma-Assisted Atomic Layer Deposition. *J. Korean Phys. Soc.* **2013**, *62*, 1143–1149. [CrossRef]
18. Egorov, K.V.; Kuzmichev, D.S.; Sigarev, A.A.; Myakota, D.I.; Zarubin, S.S.; Chizov, P.S.; Perevalov, T.V.; Gritsenko, V.A.; Hwang, C.S.; Markeev, A.M. Hydrogen Radical Enhanced Atomic Layer Deposition of TaOx: Saturation Studies and Methods for Oxygen Deficiency Control. *J. Mater. Chem. C* **2018**, *6*, 9667–9674. [CrossRef]
19. Xu, J.; Yang, C.S.; Choi, C.K. Annealing Effects on the Structural and Electrical Properties of SiOC(-H) Films with Low Dielectric Constant Prepared by Plasma-Enhanced Chemical Vapor Deposition. *J. Korean Phys. Soc.* **2004**, *45*, 175–179.
20. Salh, R. Defect Related Luminescence in Silicon Dioxide Network: A Review. In *Crystalline Silicon-Properties and Uses*; IntechOpen: London, UK, 2011; Volume 135, p. 172. [CrossRef]
21. Dutt, A.; Salinas, R.A.; Martínez-Tolibia, S.E.; Ramos-Serrano, J.R.; Jain, M.; Hamui, L.; Ramos, C.D.; Mostafavi, E.; Kumar Mishra, Y.; Matsumoto, Y.; et al. Silicon Compound Nanomaterials: Exploring Emission Mechanisms and Photobiological Applications. *Adv. Photonics Res.* **2023**, *4*, 2300054. [CrossRef]
22. Ramos-Serrano, J.R.; Matsumoto, Y.; Méndez-Blas, A.; Dutt, A.; Morales, C.; Oliva, A.I. Luminescent Silicon Oxycarbide Thin Films Obtained with Monomethyl-Silane by Hot-Wire Chemical Vapor Deposition. *J. Alloys Compd.* **2019**, *780*, 341–346. [CrossRef]
23. Tessler, L.R.; Solomon, I. Photoluminescence of Tetrahedrally Coordinated A-Si1-XCx:H. *Phys. Rev. B* **1995**, *52*, 10962–10971. [CrossRef]
24. Güneş, İ.; Sel, K. Effects of Carbon Content and Plasma Power on Room Temperature Photoluminescence Characteristics of Hydrogenated Amorphous Silicon Carbide Thin Films Deposited by PECVD. *Thin Solid Films* **2017**, *636*, 85–92. [CrossRef]
25. Vivaldo, I.; Moreno, M.; Torres, A.; Ambrosio, R.; Rosales, P.; Carlos, N.; Calleja, W.; Monfil, K.; Benítez, A. A Comparative Study of Amorphous Silicon Carbide and Silicon Rich Oxide for Light Emission Applications. *J. Lumin.* **2017**, *190*, 215–220. [CrossRef]
26. Dutt, A.; Matsumoto, Y.; Santoyo-Salazar, J.; Santana-Rodríguez, G.; Godavarthi, S. Blue to Red Emission from As-Deposited Nc-Silicon/Silicon Dioxide by Hot Wire Chemical Vapor Deposition. *Thin Solid Films* **2015**, *595*, 221–225. [CrossRef]
27. Shluger, A.; Stefanovich, E. Models of the Self-Trapped Exciton and Nearest-Neighbor Defect Pair in SiO_2. *Phys. Rev. B* **1990**, *42*, 9664–9673. [CrossRef]
28. Walters, R.J.; Bourianoff, G.I.; Atwater, H.A. Field-Effect Electroluminescence in Silicon Nanocrystals. *Nat. Mater.* **2005**, *4*, 143–146. [CrossRef]
29. Cabañas-Tay, S.A.; Palacios-Huerta, L.; Aceves-Mijares, M.; Coyopol, A.; Morales-Morales, F.; Pérez-García, S.A.; Licea-Jiménez, L.; Domínguez-Horna, C.; Monfil-Leyva, K.; Morales-Sánchez, A. Study of Narrow and Intense UV Electroluminescence from ITO/SRO/Si-p and ITO/SRN/SRO/Si-p Based Light Emitting Capacitors. *J. Lumin.* **2017**, *183*, 334–340. [CrossRef]
30. Boulitrop, F.; Dunstan, D.J. Phonon Interactions in the Tail States of A-Si:H. *Phys. Rev. B* **1983**, *28*, 5923–5929. [CrossRef]

31. Kruangam, D.; Toyama, T.; Hattori, Y.; Deguchi, M.; Okamoto, H.; Hamakawa, Y. Improvement of Carrier Injection Efficiency in A-SiC p-i-n LED Using Highly-Conductive Wide-Gap p, n Type a-SiC Prepared by ECR CVD. *J. Non. Cryst. Solids* **1987**, *97–98*, 293–296. [CrossRef]
32. Cabanas-Tay, S.A.; Morales-Sanchez, A.; Palacios-Huerta, L.; Aceves-Mijares, M. UV Electroluminescence from ITO/SRO/p-Si and ITO/SRN/SRO/p-Si Structures. In Proceedings of the 2016 13th International Conference on Electrical Engineering, Computing Science and Automatic Control, CCE 2016, Mexico City, Mexico, 26–30 September 2016; IEEE: Piscataway, NJ, USA, 2016; pp. 1–5.
33. Sel, K.; Akaolu, B.; Atilgan, I.; Katirciolu, B. Effects of Tail States on the Conduction Mechanisms in Silicon Carbide Thin Films with High Carbon Content. *Solid. State. Electron.* **2011**, *57*, 1–8. [CrossRef]
34. Palacios-Huerta, L.; Cabanas-Tay, S.A.; Luna-López, J.A.; Aceves-Mijares, M.; Coyopol, A.; Morales-Sánchez, A. Effect of the Structure on Luminescent Characteristics of SRO-Based Light Emitting Capacitors. *Nanotechnology* **2015**, *26*, 395202. [CrossRef]
35. Chiu, F.C. A Review on Conduction Mechanisms in Dielectric Films. *Adv. Mater. Sci. Eng.* **2014**, *2014*, 578168. [CrossRef]
36. Ramírez, J.M.; Berencén, Y.; López-Conesa, L.; Rebled, J.M.; Peiró, F.; Garrido, B. Carrier Transport and Electroluminescence Efficiency of Erbium-Doped Silicon Nanocrystal Superlattices. *Appl. Phys. Lett.* **2013**, *103*, 081102. [CrossRef]
37. Lin, G.-R.; Lin, C.-J.; Kuo, H.-C. Improving Carrier Transport and Light Emission in a Silicon-Nanocrystal Based MOS Light-Emitting Diode on Silicon Nanopillar Array. *Appl. Phys. Lett.* **2007**, *91*, 093122. [CrossRef]